JCTC Journal of Chemical Theory and Computation

pubs.acs.org/JCTC Article

Interlayer Charge Transport in 2D Lead Halide Perovskites from First Principles

Wei Li,* Samuele Giannini,* Claudio Quarti, Zhufeng Hou, Oleg V. Prezhdo,* and David Beljonne

Cite This: J. Chem. Theory Comput. 2023, 19, 9403−9415 Read Online

ACCESS | Metrics & More | Article Recommendations | Supporting Information

ABSTRACT: We report on the implementation of a versatile projection-operator diabatization approach to calculate electronic coupling integrals in layered periodic systems. The approach is applied to model charge transport across the saturated organic spacers in two-dimensional (2D) lead halide perovskites. The calculations yield out-of-plane charge transfer rates that decay exponentially with the increasing length of the alkyl chain, range from a few nanoseconds to milliseconds, and are supportive of a hopping mechanism. Most importantly, we show that the charge carriers strongly couple to distortions of the Pb−I framework and that accounting for the associated nonlocal dynamic disorder increases the thermally averaged interlayer rates by a few orders of magnitude compared to the frozen-ion 0 K-optimized structure. Our formalism provides the first comprehensive insight into the role of the organic spacer cation on vertical transport in 2D lead halide perovskites and can be readily extended to functional π-conjugated spacers, where we expect the improved energy alignment with the inorganic layout to speed up the charge transfer between the semiconducting layers.

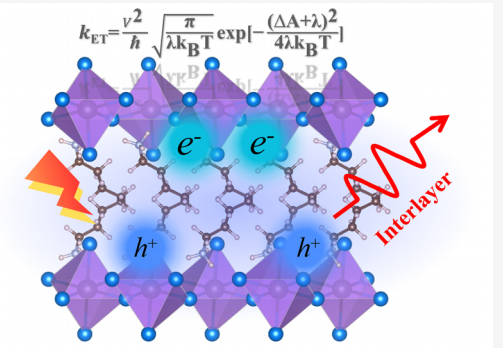

1. INTRODUCTION

Simulating charge transport in two-dimensional (2D) materials is both a scientifically relevant and challenging task.[1−3] The rapid emergence of dimensionally confined materials in strategic technological fields calls for the development of appropriate simulation tools. Their anisotropic structure, however, inherently entails the coexistence of different transport regimes, as related to in-plane versus out-of-plane transport. A striking example is represented by 2D organic−inorganic hybrid perovskites, which have attracted much attention over the past decade as promising semiconducting materials for efficient and stable photovoltaic and light-emitting applications.[4−7] 2D lead halide perovskites consist of electronically inert organic cations sandwiched between inorganic layers of corner-sharing $[PbI_6]^{4-}$ octahedra. The structural formula of the 2D perovskites is $(A')_m(A)_{n-1}B_nX_{3n+1}$, where A′ is a monovalent (m = 2) or divalent (m = 1) cation spacer corresponding to the Ruddlesden−Popper (RP) or Dion-Jacobson (DJ) families, respectively.[8] A is a small monovalent cation (methylammonium and formammidinium at the forefront) or an alkali metal (Cs), B is lead, and X is a halogen (iodine here). The integer n refers to the thickness of the inorganic layer. Despite significant progress, the power conversion efficiency (PCE) of solar cells based on 2D perovskites[9] is still lagging behind their three-dimensional (3D) counterparts,[10] in part because of their unpaired in-plane versus out-of-plane charge transport properties.[11−14] It is now widely recognized that charge transport is less efficient along the out-of-plane direction of 2D perovskites compared to the in-plane direction, owing to the mostly insulating nature of the organic spacer cations.[14−17] This results in the confinement of charges in the inorganic layers, which can seriously affect the device performance.[18] Significant effort has been devoted to the development of suitable spacer cations,[19,20] namely by reducing the energy mismatch between the organic cations' frontier molecular orbitals and the inorganic layout crystalline orbitals. While we expect the size and nature of the organic cation to strongly impact interlayer transport, to the best of our knowledge this has not been comprehensively investigated. In particular, organic cations bring their own vibrational degrees of freedom and, irrespective of the actual organic−inorganic energy level alignment,[21] it is not clear whether the increased dynamical disorder associated with the organic cations perturbs out-of-plane charge transport.

In general, the presence of saturated spacer cations entails a combined spatial and dielectric quantum confinement of the carriers.[12,17,22−24] Several reports have demonstrated that the use of shorter-chain cations can enhance the probability of charge tunneling and, thereby, benefit interlayer charge transport because of the reduced barrier width.[25] For example,

Received: August 17, 2023
Revised: October 20, 2023
Accepted: November 9, 2023
Published: December 4, 2023

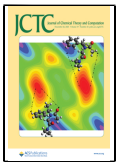

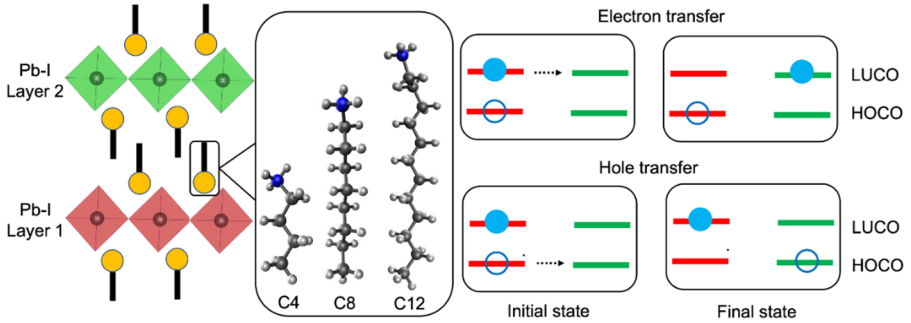

Figure 1. (left) Schematic illustration of the orthorhombic crystal structures of C4PbI, C8PbI, and C12PbI. All crystalline models contain two inorganic Pb−I layers, 1 and 2, indicated in red and green, respectively. (right) Schematic diagram for the charge transfer between different inorganic Pb−I layers in 2D perovskites. The interlayer charge transfer corresponds to the transfer of a photoexcited electron (or hole) from the LUCO (or HOCO) of layer 1 to the LUCO (or HOCO) of layer 2. Charge transfer can also occur from layer 2 to layer 1 following a similar mechanism.

replacing the *n*-butylammonium (*n*-BA) spacer with shorter-branched *iso*-butylammonium (*iso*-BA) in 2D perovskites has been shown to boost the out-of-plane carrier mobility from less than 0.01 to 1.35 $cm^2\ V^{-1}\ s^{-1}$.[13] *Iso*-BA produces interlayer charge transfer twice as fast as *n*-BA, with both time scales in the few hundreds ps range,[26] which agrees with previous reports.[6,27,28] Zhu and co-workers reported an enhanced out-of-plane charge transport in 2D perovskites via the fluorination of the phenethylammonium (PEA) spacer.[29] Fluorine substitution of the PEA spacer cation likely enhances the intermolecular H-bonding and $\pi-\pi$ stacking, decreases the interlayer spacing, and strengthens the interlayer interactions, in turn leading to increased vertical charge carrier mobility.[29] All of these observations point to the influence of the organic cation length and nature on the interlayer charge transport in 2D perovskites.

From a theoretical perspective, vertical charge transport in 2D perovskites is still a relatively unexplored area. Several computational works have screened potential 2D perovskite candidates by estimating the carrier effective mass along the out-of-plane direction.[30,31] Other groups have investigated the chemical interactions between spacer cations and the inorganic layer in 2D perovskites using first-principles calculations.[32−34] The Rothlisberger group proposed a simple barrier model to quantify the interlayer tunneling probability of 2D perovskites.[35] The insulating nature of the spacer cation is reflected by the rather small tunneling probability in the out-of-plane direction. Zhang and co-workers further investigated the out-of-plane carrier transport in a series of ideal 2D lead halide perovskites (LHPs) via first-principles calculations.[36] They found that interlayer reduction associated with the substitution of bulky spacers (butylammonium or phenethylammonium) with small cations (methylammonium and formamidinium) led to an increase of the interlayer carrier tunneling probability by about 2 orders of magnitude. Very recently, Scholes and co-workers carried out combined experimental and theoretical investigations on 2D layered perovskites and concluded that interlayer exciton transfer is much faster than free carrier charge transfer.[37] The above works have provided timely insights into the interlayer charge transport in 2D perovskites. Nevertheless, a comprehensive understanding of the out-of-plane charge transport dynamics in 2D layered perovskites still needs to be achieved, in part due to the lack of an appropriate computational framework.

In this work, we studied interlayer charge transfer in 2D halide perovskites from analytic rate constants using both Marcus and semiclassical Landau−Zener theories.[38] As we discuss below, employing well-established Marcus equations offers an especially effective framework for examining the charge transfer rates between layers that can be regarded as distinct localized (quasi-diabatic) states. These states consist of an initial configuration with the charge located at the first layer and a final configuration with the charge positioned at the second layer (Figure 1). Broadly speaking, this depiction holds true when the electronic interactions (referred to as electronic couplings) between these layers are significantly smaller than the reorganization energy (the energy expense required to transition the neutral configuration of the final state to match that of the initial state while maintaining the same electronic configuration). The core of this work is to extract the necessary parameters, namely the interplane electronic couplings, by adopting the projection-operator diabatization (POD) approach[39,40] in conjunction with electronic structure calculations and ab initio molecular dynamics (MD) to take into account the important effect of thermal fluctuations. To ease the definition of localized states, we resort to periodic density functional theory (DFT) within numerically atomic orbital (AO) formalism, as implemented in the OpenMX code.[41,42] This allows us to bypass alternative nontrivial procedures for the definition of a localized wave function. In principle, however, a similar procedure could be carried out using non-atom-centered bases, for instance, by exploiting the Wannierization of the initial Bloch states.

We apply our procedure to investigate the out-of-plane charge transport in 2D perovskites with variable alkyl chain lengths. Specifically, we focus on 2D RP perovskites with A′ being $C_4H_9NH_3$ (butylaminium), $C_8H_{17}NH_3$ (octylaminium), and $C_{12}H_{25}NH_3$ (dodecylaminium), as shown in Figure 1. For simplicity, we abbreviate these compounds as C4PbI, C8PbI, and C12PbI, respectively, and the corresponding spacer cations are C4, C8, and C12, respectively. The simulations indicate that the organic cation length influences the relative rotation and tilting of the $[PbI_6]^{4-}$ octahedra in the inorganic layers, which in turn influence the orbital hybridization between the Pb 6s and I 5p states. The use of a longer alkyl chain spacer cation translates into an increased interlayer spacing and, thus, a reduced interlayer coupling, leading to a wider tunneling barrier and slower out-of-plane charge transport. Very interestingly, we found that while simulations on static X-ray diffraction (XRD) structures predict infinitely slow interlayer charge transfer, while the inclusion of thermally induced nuclear motion via molecular dynamics (MD)

https://doi.org/10.1021/acs.jctc.3c00904
J. Chem. Theory Comput. 2023, 19, 9403−9415

simulations yields a large (2−3 orders of magnitude) increase in thermalized hopping rates. In addition to bringing theory in closer agreement with available experiments, the present findings pinpoint the central role of finite temperature effects in the interlayer charge transfer mechanism in 2D halide perovskites.

2. METHODS

2.1. Interlayer Electron Couplings from Projection-Operator Diabatization (POD). We give here a brief overview of the salient features of the POD approach for the estimation of the interlayer couplings (full details can be found in ref 40). We start by expressing the Kohn−Sham matrix (H) for a periodic system in an atomic-centered basis representation:

$$H(\mathbf{k}) = \sum_n e^{i\mathbf{k}\mathbf{R}_n} \langle \phi_i(\mathbf{r}) | H | \phi_j(\mathbf{r} - \mathbf{R}_n) \rangle \tag{1}$$

where $\mathbf{k}$ is a given crystal momentum, $\mathbf{R}_n$ is a real space translation vector of the crystal, and ϕ_i denotes the atomic orbitals. The Kohn−Sham matrix H is determined here self-consistently by using the OpenMX code. Non-orthogonality of the atomic-centered basis function is generally not a problem, as one can invoke the Löwdin transformation to transform the initial basis ($B = \{\phi_i\}$) into a new basis ($\tilde{B} = \{\tilde{\phi}_i\}$):

$$|\tilde{\phi}_i\rangle = \sum_j S_{ji}^{-1/2} |\phi_j\rangle \tag{2}$$

where S_{ij} denotes the AO overlap through the matrix elements $\langle \phi_i | \phi_j \rangle$. Such a transformation preserves the localization features for the new basis functions. The Kohn−Sham matrix in the Löwdin orthogonal basis becomes

$$\tilde{H} = S^{-1/2} H S^{-1/2} \tag{3}$$

For a donor (D)−acceptor (A) system, the Kohn−Sham matrix in eq 1 can be block partitioned based on the spatial location of the basis functions. In the case of the 2D perovskites, we cast down the reference cell sketched in Figure 1 into two fragments, each consisting of an inorganic layer and the monovalent spacer cations required to guarantee charge neutrality. With reference to crystal structures from Billing and Lemmerer,[43−45] each layer within the unit cell is composed of two $[PbI_6]^{4-}$ octahedra and four spacer cations, the two fragments being equivalent due to the space group symmetry. The partition of the total basis $\tilde{B}$ into donor and acceptor subsystems produces the subsets $\tilde{B}_D$ and $\tilde{B}_A$, satisfying

$$\tilde{B}_D \cup \tilde{B}_A = \tilde{B}; \quad \tilde{B}_D \cap \tilde{B}_A = \emptyset \tag{4}$$

The subsets $\tilde{B}_D$ and $\tilde{B}_A$ consist of N_D and N_A basis functions, respectively (in this case, N_D and N_A are the same for the two layers). It is convenient to order the basis function, $\tilde{\phi}_i$, according to their assignment to the subsystems. This leads to the following definitions of the subsets:

$$\tilde{B}_D = \{\tilde{\phi}_i : i \in [1; N_D]\} \tag{5}$$

$$\tilde{B}_A = \{\tilde{\phi}_i : i \in [N_D + 1; N_A]\} \tag{6}$$

Let T_D and T_A be the transformations that diagonalize respectively the sub-blocks $\tilde{H}_{DD}$ and $\tilde{H}_{AA}$ associated with the donor and acceptor subsystems. The application of the following unitary transformation T to the full Kohn−Sham matrix

$$H' = T^+ \tilde{H} T = \begin{bmatrix} T_D^+ & 0 \\ 0 & T_A^+ \end{bmatrix} \begin{bmatrix} \tilde{H}_{DD} & \tilde{H}_{DA} \\ \tilde{H}_{AD} & \tilde{H}_{AA} \end{bmatrix} \begin{bmatrix} T_D & 0 \\ 0 & T_A \end{bmatrix} \tag{7}$$

leads to a Hamiltonian H' in the form

$$H' = \begin{bmatrix} \varepsilon_{1,D} & 0 & & & & & & \\ 0 & \varepsilon_{2,D} & & & & V_{DA} & & \\ \vdots & & \ddots & & & & & \\ & & & \varepsilon_{n,D} & & & & \\ & & & & \varepsilon_{1,A} & 0 & & \\ & & V_{AD} & & 0 & \varepsilon_{2,A} & & \\ & & & & \vdots & & \ddots & \\ & & & & & & & \varepsilon_{n,A} \end{bmatrix} \tag{8}$$

The diagonal blocks of H' consist of diagonal matrices containing elements defined as

$$\varepsilon_{DD} = T_D^+ \tilde{H}_{DD} T_D; \quad \varepsilon_{AA} = T_A^+ \tilde{H}_{AA} T_A \tag{9}$$

These correspond to the energies ε_D and ε_A of the diabatic states associated with the donor and the acceptor, respectively.

The off-diagonal blocks instead contain elements defined as

$$V_{DA} = T_D^+ \tilde{H}_{DA} T_A; \quad V_{AD} = T_A^+ \tilde{H}_{AD} T_D \tag{10}$$

corresponding to the coupling between the diabatic states of the donor and acceptor.

In principle, the off-diagonal elements of the Hamiltonian should be dependent on the momentum $\mathbf{k}$-space (eq 1), and we can extend the calculation of electronic coupling into arbitrary $\mathbf{k}$-points. However, here we focus exclusively on the Γ point, where the top of the valence band and the bottom of the conduction band are located; see the band structure in Figure S1. Then, the phase factor term $e^{i\mathbf{k}\mathbf{R}_n} = 1$. The off-diagonal elements of the Hamiltonian not calculated in Γ would no longer be informative of the frontier states, which are more interesting for the interlayer charge transport mechanism in the studied systems.

The above procedure that was used to obtain electronic coupling can be applied to a wide range of systems, including molecular crystals, periodic solids, infinite periodic surfaces, etc.[39,40] The POD procedure is suitable for obtaining couplings between diabatic states in different situations schemes, such as, for instance, in connection with MD simulations. See section 2.3 for details about the ab initio MD simulations performed in this work. The super-exchange mechanism, which is the key mechanism for long-range charge transfer across organic spacers that have no energy levels close to the energies of the donor and acceptor states,[46] is also accounted for in the current POD approach. The donor and acceptor are coupled through the spacer bridge states. The performed POD method considers layer 1 and layer 2 (as shown in Figure 1), in which the spacers are included, thus providing an intermediate and the most practical representation compared to both the adiabatic representation and an alternative possible donor/bridge/acceptor diabatization representation. In particular, the nonadiabatic coupling arising from the adiabatic representation is hard to compute for numerical reasons (it can rapidly diverge when adiabatic states become quasi-degenerate). The donor/bridge/acceptor diabatization is more complex and less rigorously defined than the layer 1/layer 2 POD.

2.2. Analytic Rate Constants. *Marcus Theory.* Coupling from the POD method can be used in connection with Marcus theory,[47] which has been widely applied to model electron transfer in the condensed phase.[48] In weak coupling and the high-temperature classical limit ($\hbar\omega \ll k_B T$), which applies to

https://doi.org/10.1021/acs.jctc.3c00904
J. Chem. Theory Comput. 2023, 19, 9403−9415

the current systems (as confirmed below), the rate constant (k_{Marcus}) for nonadiabatic charge transfer can be written as

$$k_{Marcus} = \left(\frac{V_{kl}^2}{\hbar}\right)\sqrt{\frac{\pi}{\lambda k_B T}}\ \exp\left(-\frac{(\Delta A + \lambda)^2}{4\lambda k_B T}\right) \quad (11)$$

Here, V_{kl} is the electronic coupling between the diabatic states k and l. This is estimated using the POD method on geometries taken from XRD measurements as well as on snapshots extracted from an ab initio MD simulation to incorporate the effect of thermal fluctuations. In the latter case, the coupling in eq 11 is substituted by its thermal average by considering the variance of the coupling fluctuations (σ_V^2):

$$\langle V_{kl}^2\rangle = \langle V_{kl}\rangle^2 + \sigma_V^2 \quad (12)$$

In eq 11, ΔA is the electron transfer barrier height. In this work, this quantity is set to zero, as the two layers in C4PbI, C8PbI, and C12PbI are equivalent, as indicated by the symmetry of the *Pbca* space group. Finally, λ is the reorganization energy related to the local electron−phonon coupling, namely the modulation of the site (i.e., layer) energies due to electron−vibrational interactions. Different strategies can be used to calculate this quantity.[49−51] An insightful approach relies on calculating the spectral density ($J(\omega)$) of the vertical energy gap fluctuations in real time: $\delta\Delta E(t) = \Delta E(t) - \langle\Delta E\rangle_M$ (where the bracket denotes thermal averaging in a given state M), as obtained, for instance, here from ab initio MD simulations. In this work, we approximate the vertical energy gap by using the orbital energy difference associated with the highest occupied/lowest unoccupied crystalline orbitals (HOCO/LUCO) of each layer. This allows us to determine the energetic disorder, $\sigma_E^2 = \langle(\delta\Delta E)^2\rangle_M$.[52] In the classical limit, the reorganization energy is

$$\lambda = \frac{2}{\pi}\int_0^\infty \frac{J(\omega)}{\omega}\,d\omega = \frac{\sigma_E^2}{2k_B T} \quad (13)$$

where $J(\omega)$ is obtained by a cosine transform of the site energy fluctuations:

$$\frac{J(\omega)}{\omega} = \frac{1}{2k_B T}\int_0^\infty dt\ \langle\delta\Delta E(0)\delta\Delta E(t)\rangle_M \cos\omega t \quad (14)$$

Equation 14 is very useful because it allows one to understand the reorganization energy property in terms of the contributions from different frequencies, ideally ascribable to specific phonons/normal modes more strongly coupled to energy variations. The Marcus theory expression discussed above is justified when the electronic coupling is much smaller than the reorganization energy. A more general semiclassical (SC) rate expression can be derived by combining the transition state theory in the harmonic approximation and the Landau−Zener theory for electron transfer from an initial diabatic state to a final state as discussed in SI, Section S1.

2.3. Electronic Structure Calculations. For all of the investigated systems, we used the unit cell of the orthorhombic phase model (*Pbca*, space group 61) reported by Billing in refs 43−45 and 53. The unit cell of these models have been successfully used in previous theory works for either static calculations[33] or ab initio nonadiabatic molecular dynamics simulations.[54,55] The use of a larger cell size would require the diagonalization of a large fragment Hamiltonian, and repeated full-dimensional Hamiltonian diagonalization would be prohibitive. Geometry optimization at 0 K and adiabatic Born−Oppenheimer MD simulation at finite temperature were carried out using the VASP code,[56] employing the projector-augmented wave pseudopotentials. The plane-wave energy cutoff was set to 400 eV. A Monkhorst−Pack **k**-point mesh of 5 × 5 × 1 was used for both the geometry optimization and MD simulations, the anisotropic sampling of the reciprocal space reflecting the larger lattice parameter associated with the plane stacking direction. The van der Waals interactions were described by the DFT-D2 method proposed by Grimme.[57] We first relaxed both atomic positions and lattice parameters of the C4PbI, C8PbI, and C12PbI compounds at 0 K. Atomic positions were considered fully relaxed when all forces were below 0.01 eV/Å. We then performed MD simulations in the canonical ensemble (NVT) for 10 ps with the target temperature maintained by a Nosé−Hoover chain thermostat applied at 300 K, corresponding to the operating conditions of perovskite solar cells. A time step of 1 fs was used, which allowed us to sample high-frequency modes (N−H). The first 7 ps of the trajectory of each system are considered as the thermalization and disregarded, while the last 3 ps are used to extract electronic couplings in real time, following the POD procedure (eqs 7−10), and the relaxation energy (eqs 13 and 14). To this aim, we used the OpenMX software package (version 3.9)[41,42] to extract the Kohn−Sham matrix and the overlap matrix at the Γ **k**-point. Calculations were performed with the Perdew−Burke−Ernzerhorf (PBE) exchange-correlation functional.[58] H6.0-s2p1, C6.0-s2p2d1, N6.0-s2p2d1, I7.0-s3p2d2f1, and Pb8.0-s3p2d2f1 pseudoatomic orbitals were used. A Monkhorst−Pack **k**-point mesh of 2 × 2 × 1 was adopted for the following POD procedure.

The accurate estimate of the band gap of 2D halide perovskites requires both the inclusion of spin−orbit coupling and a proper description of many-body interactions, as from the *GW* approximation or hybrid DFT.[33,59,60] Conversely, such level of theory is unaffordable in the present case due to the need of repeatedly performing thousands of electronic structure calculations to estimate the electronic couplings and site energies along the MD trajectory.[61] Still, it is worth stressing that this work focuses on the interlayer charge transfer process in 2D halide perovskites. This is more sensitive to the energy level alignment between the states of the organic and inorganic components and the related energy offset than to the absolute band gap of these compounds. A previous work confirmed that standard PBE calculations correctly predicts type-I energy level alignment at the organic/inorganic interface,[21] as is also confirmed in Figure S1. Therefore, all calculations in this work were performed with the PBE functional.

3. RESULTS AND DISCUSSION

3.1. Preliminary Analyses. The PBE-D2-optimized lattice parameters from our simulations nicely parallel the experimental data (Table S1),[43−45,53] with slight discrepancies that should be considered in light of the fact that, while static DFT refers to 0 K, the experimental data were recorded at a finite temperature. Figure S2 shows the optimized unit cells of C4PbI, C8PbI, and C12PbI. The dependence of the lattice constants on the organic cation is as follows: the values of a and c increase gradually from C4PbI to C8PbI to C12PbI, whereas b shows the reverse trend. The change in parameter c is more profound and directly reflects the increasing length of the organic cation chain. We also note that the distortion related to the octahedral rotation, as probed from the Pb−I−

https://doi.org/10.1021/acs.jctc.3c00904
J. Chem. Theory Comput. 2023, 19, 9403−9415

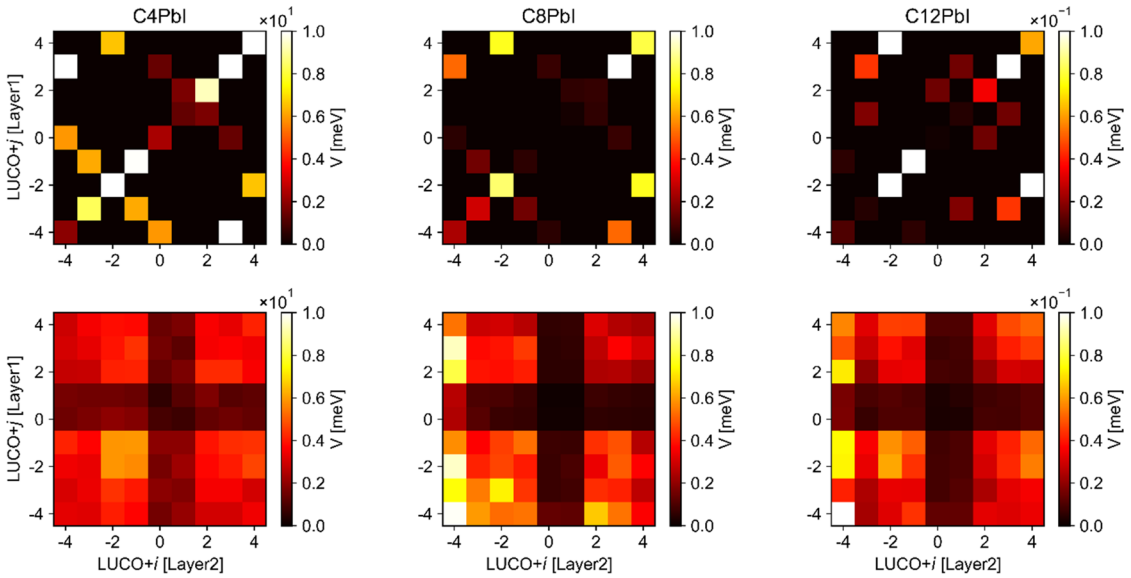

Figure 2. 2D maps of the absolute valued electronic coupling (in units of meV) for the (top) 0 K structure and (bottom) canonical averaged at 300 K. We represent the coupling between different orbitals, taking as a reference the LUCO of the three investigated systems, as indicated.

Table 1. Parameters for Interlayer Charge Transfer Computed for the Investigated 2D Layered Perovskites and Corresponding Transition Rates and Mobilities[a]

		V_{kl} (meV)	$\langle V_{kl}^2\rangle^{1/2}$ (meV)	σ_V (meV)	λ (eV)	τ_{Marcus}	μ_{hop} (cm^2 V^{-1} s^{-1})
C4PbI	L	8.7×10^{-2}	1.10	1.08	0.83	137.6 ns	4.46×10^{-6}
	H	0.36	7.44	7.41	1.08	38.5 ns	1.59×10^{-5}
C8PbI	L	1.38×10^{-4}	1.73×10^{-2}	1.72×10^{-2}	0.97	2.3 ms	6×10^{-10}
	H	1.98×10^{-3}	0.73	0.65	0.54	18.8 ns	7.35×10^{-5}
C12PbI	L	4.34×10^{-5}	3.2×10^{-3}	3×10^{-3}	1.18	572.0 ms	3.99×10^{-12}
	H	3.95×10^{-3}	6.46×10^{-2}	6.43×10^{-2}	1.11	690.2 μs	3.31×10^{-9}

[a]HOCO−HOCO (H) and LUCO−LUCO (L) electronic couplings for the 0 K structures (V_{kl}) and canonically averaged electronic couplings from the MD simulations ($\langle V_{kl}^2\rangle^{1/2}$), along with its standard deviation (σ_V); the averaged reorganization energy (λ); the hole and electron hopping time obtained from Marcus theory (τ_{Marcus}); and the carrier mobility calculated based on the Marcus hopping rate (μ_{hop}).

Pb valence bond, evolves non-monotonically with the spacer length (see Table S2) with C12/C8 being the most/less distorted system. The penetration depth of the organic cation into the inorganic network can be qualitatively revealed by the degree of distortion of the inorganic octahedra. The data presented in Table S2 show that the spacer cation with the longest organic chain length, C12, induces the largest distortion of the in-plane Pb−I−Pb angles. This is explained in ref 33 in terms of the competitive interactions between the inorganic and organic lattice, with the latter becoming dominant for longer chains.

In the presence of fully saturated or small aromatic spacers, the valence and conduction bands of 2D halide perovskites are governed by the inorganic sublattice, with the organic spacer only playing an indirect influence through induced structural distortions and electrostatic effects.[17] This is once more confirmed here for C4PbI; see Figure S1. The band gap increases nonmonotonically with chain length from C4/C8 (2.13/2.11 eV) to C12 (2.34 eV), which is in line with the experimental investigations.[23,62] It roughly follows the increasing structural distortion of the inorganic frame (see the Supporting Information (SI)), as measured by the Pb−I−Pb angle,[63] when going to longer spacers. The highest occupied crystalline orbital (HOCO) is primarily composed of the antibonding hybridization of the Pb 6s/I 5p orbitals. In contrast, the lowest unoccupied crystalline orbital (LUCO) is mainly made up of the nonbonding Pb 6p orbitals with a minor contribution from the I 5p orbitals in antibonding hybridization.[64,65]

Additional analyses of the MD trajectories at 300 K are reported in the SI. These refer to the interaction between the organic and inorganic components of the 2D perovskites, as analyzed following the rotational autocorrelation function of the C−N vector and the vibrational power spectrum (Figure S3). The autocorrelation function of C−N points out the more rapid reorientation of the methyl group for the spacer from C4PbI4 compared to the other compounds. In all cases, the rotations of the C−N vector are constrained within a cone of 10° due to the steric hindrance imposed by the dense packing of the spacers in 2D perovskites. The vibrational power spectra confirm the fact that the inorganic frame vibrates at a low frequency, specifically <120 cm^{-1} (Figure S4).[66−74]

3.2. Hamiltonian Parameters: Interlayer Couplings. We now turn our attention to the electronic coupling between layers, as provided by the POD formalism. Couplings are represented in Figure 2 as 2D maps, indicating the interaction of the diabatic state i of layer 1 with the state j of layer 2, considering the crystalline orbitals in close to the band edge. Couplings are shown for both the static 0 K case and the finite temperature case, in which the latter couplings are estimated as ensemble-averaged values from the 3 ps MD trajectory at 300 K (eq 12). Note that only the absolute values are reported.

https://doi.org/10.1021/acs.jctc.3c00904
J. Chem. Theory Comput. 2023, 19, 9403−9415

The couplings are generally small, typically on the order of 10^{-2} to 10^{-5} eV, and increase from 10^{-5} to 10^{-3} and 10^{-2} eV when going from the longer C12 spacer to the shorter C8 and finally to C4. Longer organic cations decrease the electronic coupling by several orders of magnitude, as the amplitude of a quantum mechanical wave function vanishes exponentially with increasing distance. For comparison, typical values for molecular organic semiconductors are usually on the order of several tens of meV or even larger.[75]

For the 0 K structure, the 2D maps are symmetric because the two inorganic Pb−I layers are equivalent for equivalent space groups. In contrast, the 2D maps are not symmetric for the electronic couplings calculated at 300 K because of thermal fluctuations.[76−78] We also observe that the hole transfer coupling is 1−2 orders of magnitude larger than the electron transfer coupling, as shown in Table 1. This is explained from a symmetry analysis in terms of different contributions from the apical iodines in the atomic hybridization of the HOCO and LUCO states. Assuming a D_{4h} point group symmetry, terminaliodines contribute to the HOCO via the out-of-plane polarized p orbitals, while they contribute to the LUCO only via the in-plane polarized p orbitals, whose orientation does not allow an effective hybridization of the Bloch states of adjacent inorganic sheets (see Figure S5).[65] The present argument is clearly no longer rigorous in the presence of octahedral-tilting, ubiquitous in 2D halide perovskites, but deviation from D_{4h} symmetry may be regarded as a perturbation. Therefore, in layered perovskites, the interplanar charge transfer should be more favorable for holes than for electrons. We note in passing that, such geometrical considerations influencing the charge density distribution of band edge states do not hold for 3D halide perovskites, as there are no such terminating halogen atoms as in the interlayer region of 2D perovskites.[65]

Remarkably, thermal fluctuations are found to enhance the electronic coupling values (see Table S3) by roughly 2−3 orders of magnitude over those of the static structures at 0 K. This suggests that thermal fluctuations play an important role in the interlayer charge transfer mechanism in 2D layered perovskites and that an accurate simulation scheme must take them into account. The interlayer HOCO−HOCO and LUCO−LUCO couplings, as estimated from the MD simulations at room temperature (300 K), show exponential decay with the distance between the donor and acceptor moieties, d (taken as the center-of-mass distance between the two layers): $V \propto e^{-\beta d}$ (see Figure 3). A linear regression of the data gives the falloff parameter (β) in the range of 0.4−0.5 Å^{-1}; these values are of the same order of magnitude as the falloff parameter estimated for donor−acceptor systems such as DNA bridges (i.e., 0.4−1.2 Å^{-1} based on conjugated linkers)[79,80] and molecular wires (i.e., 0.28−0.37 Å^{-1} in cyclic polyenes).[81,82]

Figure 4 reports the distributions of the squared electronic couplings calculated between the HOCOs/LUCOs at 300 K. The hole transfer coupling shows stronger fluctuations than the electron transfer coupling because HOCOs have more antibonding interlayer hybridizations of Pb 6s/I 5p orbitals than LUCOs. Thus, HOCOs are more sensitive to changes in orbital shapes and fluctuations in the inorganic lattice. A further examination of the standard deviation of the electronic coupling distribution (σ_V) (see Table 1) allows us to assess the role of nonlocal electron−phonon (e−ph) interactions on charge transport. The smaller σ_V that was found for the longer chains evidences a weaker interlayer interaction.

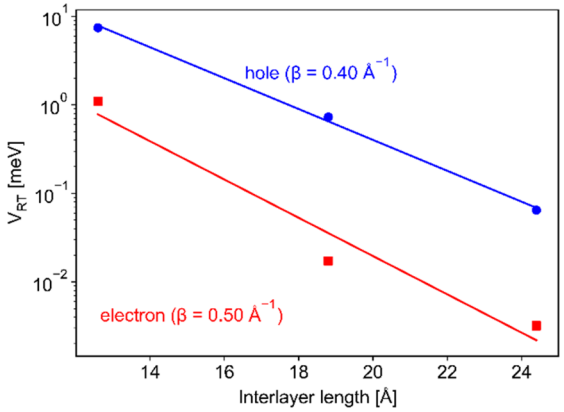

Figure 3. Dependence of interlayer HOCO−HOCO (blue squares) and LUCO−LUCO (red squares) interactions (representing hole and electron transfer couplings, respectively) of C4PbI, C8PbI, and C12PbI, as computed at 300 K, with respect to the interlayer distance. The solid lines correspond to an exponential length dependence with the falloff parameter β.

Typically, e−ph interactions can be separated in terms of local and nonlocal contributions. The two terms represent different physical pictures. Local e−ph coupling describes the modulation produced by the nuclear vibrations on the site energies (in this work, the sites are the individual layers), whereas nonlocal e−ph coupling stems from the modulation of the electronic couplings between different layers. The local and nonlocal e−ph couplings are associated with intralayer and interlayer vibrations (lattice phonons) that respectively couple to the electronic states which are involved in the charge transport. As a result, the local electron−phonon interaction induces the localization of the charge carrier on one layer, whereas the nonlocal e−ph interaction is modulated by considerable lattice disorder at a finite temperature. Standard deviations of the fluctuations of site energies and electronic coupling provide a measurement of the individual contribution of local and nonlocal e−ph coupling. Thus, the term "nonlocal dynamical disorder" means the lattice dynamical disorder induced by nonlocal e−ph interactions through the modulation of lattice phonons. Accounting for thermal fluctuations on local and nonlocal disorder has important consequences on the magnitude of the charge carrier mobility. For instance, this contribution has been studied in systems featuring both covalent and noncovalent interactions, i.e., molecular crystal/polymers.[83,84] In this work, we discuss the impact on thermal fluctuations also for 2D layered systems. We note that such analysis is not readily possible for 3D bulk perovskites, as there is no clear definition of the building blocks, namely, the fragments with both covalent/noncovalent interactions.

3.3. Real-Time Fluctuation of the HOCO/LUCO Site Energies. Site energies associated with the orbitals of the individual layers are crucial to define both relaxation energies needed for the Marcus rate equation (eq 11) and semiclassical theory (eq S1). The energy level diagrams of the static structures from DFT optimization of the C4PbI, C8PbI, and C12PbI unit cells, as obtained via the POD procedure, are shown in Figure S6. The diabatic energies of layer 1 and layer 2 are denoted as dia1 and dia2, respectively. The adiabatic energies of the total system as well as the eigenvalues obtained by diagonalizing H' of eq 8 are also shown for comparison. We first stress that diagonalizing H' fully recovers the adiabatic energies of the total system, demonstrating the reliability of the

https://doi.org/10.1021/acs.jctc.3c00904
J. Chem. Theory Comput. 2023, 19, 9403−9415

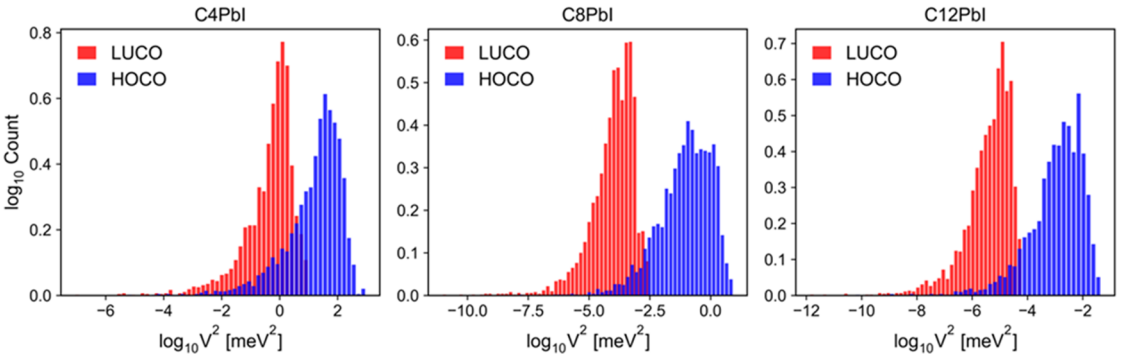

Figure 4. Histograms of the distributions of the squared electronic couplings for LUCO and HOCO.

POD procedure implemented in this work. We further find that the diabatic energies of both layers are degenerate at 0 K, which is consistent with the fact that the two inorganic layers are equivalent for space group symmetry. This degeneracy is expected to break at finite temperature MD simulations due to random structural fluctuations.[85] Generally, the diabatic HOCO of each layer from POD lies at a higher energy than the adiabatic HOCO state for the whole system. We attribute this to the fact that the diabatized states of one layer still interact with the other layer via the off-diagonal blocks V_{DA} in eq 8. Therefore, to avoid potential artifacts associated with the POD procedure on the estimate of the site energies and their corresponding real-time fluctuations, we recomputed the orbital site energies by performing independent self-consistent DFT calculations on the individual layers, as extracted from the crystalline cell. To investigate the charge transport, we mainly focused on crystalline orbitals that mediate charge transfer, that is, the HOCO for hole transfer and the LUCO for electron transfer (see Figure 1).

Figure 5 shows the real-time diabatic HOCO and LUCO site energies during the MD simulation at 300 K. The orbital

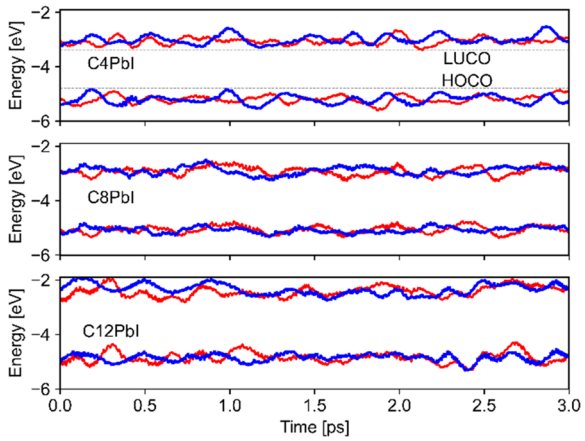

Figure 5. Time evolution of diabatic HOCO and LUCO energies for layer 1 (red) and layer 2 (blue) of the C4PbI, C8PbI, and C12PbI compounds.

energies of the two layers fluctuate continuously, which hinders a favorable energy alignment between the donor and acceptor states. As a result, quantum coherence is lost, and charge transfer is slowed down, hence leading to an interlayer charge transfer process occurring in the hopping regime. As explained in some detail when considering charge hopping along linear stacks of sites, the charge initially resides on one layer and has only a favorable time window to hop to another layer when the energy alignment of the two sites is within the resonance window imposed by twice the electronic coupling value.[86] Figure 6 depicts the energy distributions for the diabatic HOCO and LUCO states during the MD simulation, which roughly follow Gaussian distributions. The energetic disorder measured by the standard deviation of the orbital energy difference of the two layers, σ_E, is an important parameter that determines the reorganization energy (Table 1) according to the classical linear response relation (eq 13).[49] A large energetic disorder translates to a large reorganization energy and the formation of energetic barriers among adjacent hopping sites, limiting charge diffusion. σ_E is estimated for the studied layered perovskites falls in the range of 160−240 meV, with C12 showing the largest reorganization energies. This is roughly in line with the wider distribution of the values assumed by the Pb−I−Pb angles during the MD trajectories (Figure S7). The corresponding reorganization energies (λ) for the electron transfer in the investigated perovskite systems are reported in Table 1. They are 5−7 times larger than the λ values of some of the best molecular organic semiconductors (e.g., rubrene[87] and pentacene).[88] Such large reorganization energies suggest the appearance of polarons that are delocalized within the layers, yet almost completely localized between the layers of these perovskite materials. We note in passing that the λ values calculated in this work are in line with previous investigations[50,89] performed on very well-studied methylammonium lead iodide ($MAPbI_3$) and other organic−inorganic hybrid perovskite systems.

The fluctuations of the diabatic energy difference in Figure 5 can be analyzed in terms of the frequency resolved contributions, $J(\omega)$, by estimating the spectral density function (eq 13). This leads to the results in Figure 7. The running integral of the spectral density function yields the cumulative disorder, $\sigma_E(\omega)$, including all frequencies up to ω, and provides the relative contribution of each frequency interval:[90]

$$\sigma_E(\omega) = \left[\frac{4k_BT}{\pi}\int_0^{\omega}\frac{d\omega\, J(\omega)}{\omega}\right]^{1/2} \quad (15)$$

where $J(\omega)$ is the spectral density function (eq 13). An important condition from this analysis is that the integration of eq 15 over the full range of frequencies ($\omega \to \infty$) must return the standard deviation of the time series, which we verified here. Figure 7 shows that the majority of the frequencies contributing to the energetic disorder lie in the low-frequency range (<200 cm^{-1}), which is associated with the inorganic frame (see Figure S4).[91] In contrast, contributions from modes

https://doi.org/10.1021/acs.jctc.3c00904
J. Chem. Theory Comput. 2023, 19, 9403−9415

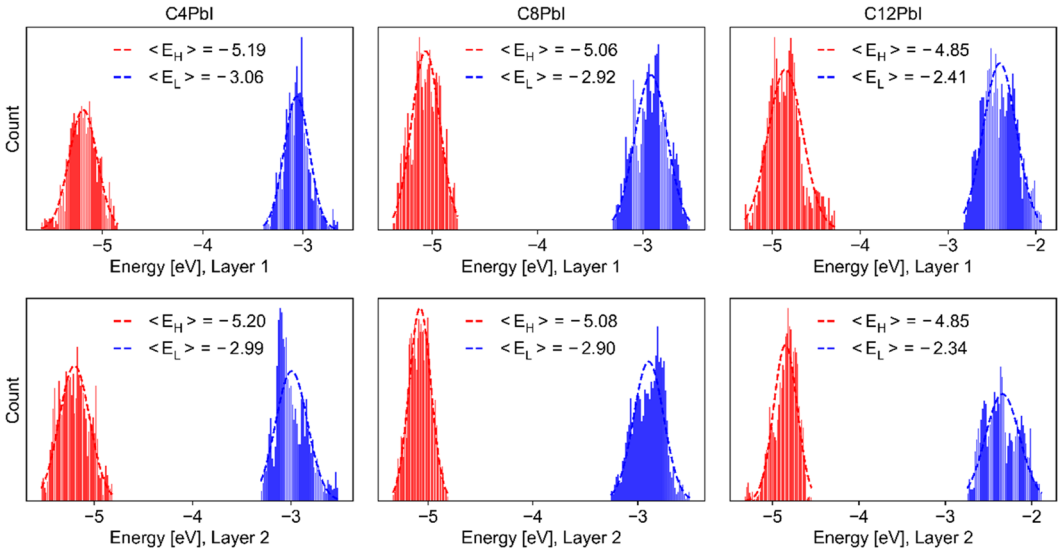

Figure 6. Histograms of the HOCO (red) and LUCO (blue) energy distributions for the energy of layer 1 (top) and layer 2 (bottom). Gaussian fits are shown with dashed lines, and the corresponding average is indicated by $\langle E_{H/L} \rangle$ (in eV).

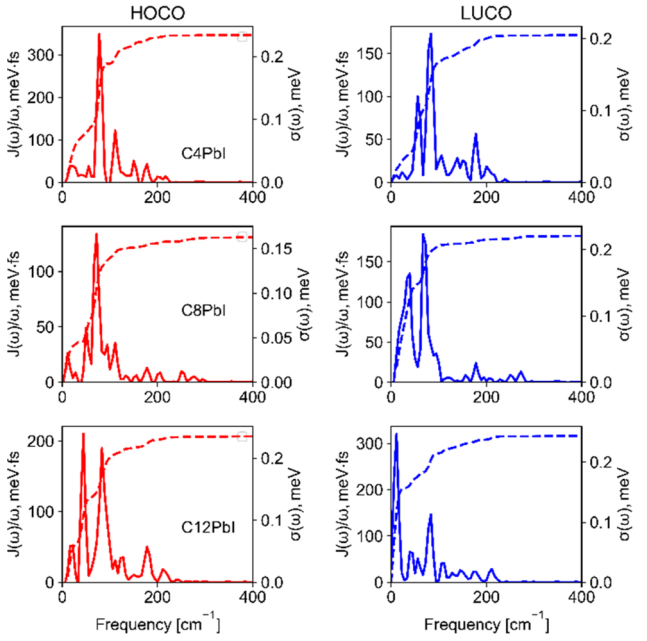

Figure 7. Spectral density functions and cumulative disorder, $\sigma_E(\omega)$, for time-dependent HOCO and LUCO energy fluctuations.

>200 cm^{-1} are negligible. This indicates that the relaxation energy is associated with distortions of the inorganic lattice, which is consistent with the quantum well electronic structures of these compounds. The key contributing frequency signals are similar for all three systems with C12PbI featuring the lowest frequency phonons contributing to the disorder. It can be concluded that the major phonons that contribute to the local electron−phonon coupling remain largely unchanged regardless of the alkyl chain length. We note in passing that the phonons that have been identified in our calculations are consistent with those obtained from larger simulation cells.[92]

3.4. Hole and Electron Interlayer Transfers Rates. The couplings from the POD procedure (Figures 2 and 3) and relaxation energies (Figures 5 and 6) allow one to estimate the interlayer charge transfer rate via the Marcus rate equation (eq 11). We used the reorganization energies (eq 13) along with the mean-square electronic coupling $\langle V_{kl}^2 \rangle$ (eq 12). It is important to note that small electronic couplings compared to the reorganization energy imply electron transfer occurring in the nonadiabatic regime. For the systems studied here, the maximum ratio between the electronic coupling at 300 K and the reorganization energy ($2V/\lambda$ = 0.054) is so small that charge transport should predominantly occur by hopping.[93,94] Moreover, the prevalence of low-frequency vibrations contributing to the local electron−phonon interaction, as reported in Figure 7, justifies the use of the classical high-temperature Marcus theory to calculate the charge transfer rates. The calculated time scales are reported in Table 1. Interlayer charge transfer rate estimates from semiclassical Landau−Zener theory (eq S1 in the SI) are given in Table S4. In principle, the Landau−Zener theory extends the regime of validity of the nonadiabatic Marcus theory to the adiabatic regime, as discussed in the SI, Section S1. Thus, this theory could be used for systems where the coupling between layers is stronger. In the systems analyzed in this work, we obtain a close agreement between the Landau−Zener rates and the rates from Marcus theory because of the small value of $2V/\lambda$. This confirms that the charge transfer in the investigated systems occurs in the nonadiabatic regime (see the SI, Section S1 for further discussion). Hole transfer is generally faster than electron transfer, owing to larger electronic coupling. Interestingly, the reorganization energies do not show sizable variation with alkyl chain length compared to the change of electronic coupling, thus making the electronic interaction between layers the dominating factor for the difference in the charge transfer rates. For C4PbI, the interlayer charge transfer time is about 38.5 ns for hole transfer and 137.6 ns for electron transfer. The charge carrier mobility (μ_{hop}) is related to the charge diffusion coefficient (D) in a one-dimensional chain by the Einstein relation:[95]

$$\mu_{hop} = \frac{eD}{k_B T} = \frac{ek_{Marcus}L^2}{k_B T} \tag{16}$$

where e is the unit charge, L is the distance between the center of mass of layer 1 and layer 2, and k_{Marcus} is the Marcus

https://doi.org/10.1021/acs.jctc.3c00904
J. Chem. Theory Comput. 2023, 19, 9403−9415

hopping rate. As shown in Table 1, the simulated out-of-plane charge carrier mobilities at room temperature span a wide range from $\sim 10^{-5}$ to $\sim 10^{-12}$ cm^2 V^{-1} s^{-1}, which is much smaller than the in-plane mobilities reported in experiments (~ 1 cm^2 V^{-1} s^{-1}).[96] Most notably, the out-of-plane hole mobility estimated for C4PbI is on the same order of magnitude as the experimentally reported value for this spacer (<0.01 cm^2 V^{-1} s^{-1}),[13] suggesting that out-of-plane transport in this material is essentially due to this carrier with limited contribution from electrons. We note, however, that from these calculations we cannot univocally deduce that hole transport is the predominant charge transport channel. In fact, although we found that electron transport is much lower when out-of-plane transport is considered, it might instead dominate when looking at intralayer charge transport.

The interlayer mobilities decrease as the interlayer distance increases, which is also in good agreement with previous experimental studies.[18] This indicates that the organic component has no direct influence on the vertical transport properties other than the tuning of the width of the potential barrier for charge carriers, at least in the presence of alkyl-based spacers. We emphasize that spacer cation may modulate the interlayer charge transport indirectly through perturbating the vibration of Pb−I lattice via electrostatic interaction.

Importantly, our calculations show that the inclusion of thermal fluctuations in the couplings enhances the charge carrier mobilities by 1−2 orders of magnitude compared to the hypothetical case of the frozen coupling values at 0 K. This effect has already been observed in the case of systems subject to sizable thermal disorder, where the transport of charges occurs via a hopping mechanism from one site to the next (e.g., organic molecular semiconductors and polymers).[83,86,97] Thermal fluctuations in the electronic couplings can help the charge transition from the initial to the final state by effectively enhancing the mean coupling value and the chances for the charge to be in the resonant transition state. It is worth noting that this observation is not in contrast with the charge transport mechanism in 3D bulk perovskites, where the disorder actually hinders the carrier mobility.[98,99] In fact, in these systems, the transport occurs in a different band-like regime where delocalized charges are actually scattered by electron−phonon interactions. Such scattering yields a mobility that decreases with increasing temperature in 3D bulk perovskites. However, a similar negative temperature dependence exponent has also been observed in 2D perovskites,[100,101] which at first seems incompatible with the hopping-like motion occurring in this system when considering out-of-plane interlayer transport. Such a contradiction can be resolved by considering the fact that in experiments, it is difficult to discern interlayer versus intralayer transport. The negative temperature dependence might be a consequence of band-like transport within a single layer dominating the experimental signal.

Our analysis shows that interlayer hole transfer proceeds much faster than electron transfer. The observed order of magnitude difference between the hole and electron transfer times is primarily explained in terms of the electronic couplings that describe the interaction between diabatic states. Jin and co-workers demonstrated that the 2D multilayered perovskites $(BA)_2(MA)_{n-1}PbnI_{3n+1}$ are a mixture of multiple perovskite phases, with $n = 1$, 2, 3, 4, and $\approx \infty$.[27] Using ultrafast transient absorption (TA) and time-resolved photoluminescence (PL) spectroscopy, the same authors proposed that photoinduced charge transfer happens from small n to large n phases due to favorable type-I band alignment, characterized by a time scale with fast components of several hundred picoseconds and slow components of nanoseconds.[27] However, the interlayer charge transfer between same phases (i.e., $n = 1$) is also possible, considering that the thermal fluctuation of electronic energy levels creates favorable energy alignments for charge transfer. Recent experimental work by Stupp and co-workers demonstrated that $n = 1$ layered perovskites exhibit improved out-of-plane charge transport through organic cation design.[18] Another work by Scholes and co-workers reported a time scale of 1−100 ps for free carrier charge transfer between multiple perovskite phases $(PEA)_2(MA)_{n-1}PbnI_{3n+1}$.[37] We note that it is hard to differentiate the time scale of the electron or hole transfer process from an experimental viewpoint. In this regard, our reported time scales of the interlayer hole and electron transfer processes for C4PbI ($n = 1$) are in qualitative agreement with the available experimental data.[27,37] The estimated time scales for C8PbI and C12PbI are much longer (except in the case of the hole transfer in C8PbI); however, we are not aware of any relevant experimental time scale study reported for these two systems. It is important to point out that the reorganization energy and electronic coupling are independent parameters; therefore, they can be ideally tuned individually by the choice of the spacer and fine-tuning of the interlayer distance to optimize the interlayer charge transport properties in 2D perovskites. For example, Nazarenko et al., exploited mixed guanidinium/Cs spacers to obtain an apical iodine-to-apical iodine distance of ∼4.4 Å.[102] In turn, Sourisseau successfully demonstrated the possibility of reducing the octahedral distortion in the inorganic frame, which is expected to impact the reorganization energy.[103]

4. CONCLUSIONS

We have implemented the POD approach for the calculation of electronic couplings in periodic crystals by interfacing it with the OpenMX program package. The method was used here to calculate the coupling for weakly interacting inorganic layers in 2D lead iodide perovskites, incorporating a fully saturated spacer with variable length (butyl-, octyl-, and dodecylammonium), and to estimate the out-of-plane hole and electron charge transfer rates, in connection with the Marcus theory and a semiclassical rate expression. Our results show that the interlayer charge transfer time is in the range of nanoseconds to milliseconds, which is in agreement with previous experimental work,[27,37] demonstrating the reliability of the developed protocol. A shorter alkyl chain length facilitates interlayer charge transport, as expected from the smaller extension of the potential barrier imposed by the spacer itself. In turn, a longer chain decreases the charge transfer by several orders of magnitude due to the weaker interlayer interactions and smaller electronic couplings. Our simulations indicate that hole transfer is faster than electron transfer, owing to the larger coupling integral. We also observed that low-frequency phonon modes associated with the Pb−I inorganic lattice dominate the charge transfer process. Interestingly, room-temperature thermal fluctuations greatly enhance the electronic coupling value by 2−3 orders of magnitude compared to those for the static geometry corresponding to 0 K, bringing the time scale in better agreement with experimental data. Overall, our detailed comprehensive investigation elucidates how organic spacer cations can be used to tailor the electronic and vibrational coupling between the organic and inorganic

https://doi.org/10.1021/acs.jctc.3c00904
J. Chem. Theory Comput. 2023, 19, 9403−9415

components in 2D perovskite materials for improved interlayer charge transport properties. The mechanistic understanding of the chain length-dependent interlayer charge transport in 2D perovskites provided in this study will be useful for future rational design. The computational protocol can be applied to study charge and energy transfer in other complex periodic systems, such as 2D layered structures and molecular semiconductor interfaces, in which the separation of the total system into donor and acceptor regions can be made naturally. Moreover, additional investigations on novel technologically interesting multilayered 2D perovskites[9,104,105] could be performed in the future using a similar computational framework.

■ ASSOCIATED CONTENT

Supporting Information

The Supporting Information is available free of charge at https://pubs.acs.org/doi/10.1021/acs.jctc.3c00904.

Description of Landau−Zener theory, optimized ground state structures, band structures calculated with and without spin−orbit coupling (SOC), comparison of vibrational density of states (VDOS) plots for all systems, symmetry allowed atomic orbital hybridizations, diabatic energies obtained using the block diagonalization procedure, thermal distribution of equatorial Pb−I−Pb angle, the lattice constants obtained from theory and experiments, Pb−I bond lengths and Pb−I−Pb bond angles, and calculated time scales and mobilities obtained from Landau−Zener theory (PDF)

■ AUTHOR INFORMATION

Corresponding Authors

Wei Li − *School of Chemistry and Materials Science, Hunan Agricultural University, Changsha 410128, China; Laboratory for Chemistry of Novel Materials, University of Mons, B-7000 Mons, Belgium;* orcid.org/0000-0002-9999-5081; Email: weili@hunau.edu.cn

Samuele Giannini − *Laboratory for Chemistry of Novel Materials, University of Mons, B-7000 Mons, Belgium;* Present Address: S.G.: Institute of Chemistry of OrganoMetallic Compounds, National Research Council (ICCOM-CNR), I-56124 Pisa, Italy; orcid.org/0000-0002-1094-3921; Email: samuele.giannini@umons.ac.be

Oleg V. Prezhdo − *Department of Chemistry, University of Southern California, Los Angeles, California 90089, United States;* orcid.org/0000-0002-5140-7500; Email: prezhdo@usc.edu

Authors

Claudio Quarti − *Laboratory for Chemistry of Novel Materials, University of Mons, B-7000 Mons, Belgium;* orcid.org/0000-0002-5488-1216

Zhufeng Hou − *State Key Laboratory of Structural Chemistry, Fujian Institute of Research on the Structure of Matter, Chinese Academy of Sciences, Fuzhou 350002, China;* orcid.org/0000-0002-0069-5573

David Beljonne − *Laboratory for Chemistry of Novel Materials, University of Mons, B-7000 Mons, Belgium;* orcid.org/0000-0002-2989-3557

Complete contact information is available at: https://pubs.acs.org/10.1021/acs.jctc.3c00904

Notes

The authors declare no competing financial interest.

■ ACKNOWLEDGMENTS

W.L. is grateful for the fruitful discussions with Zhenggang Lan, Linjun Wang, and Naoya Yamaguchi. W.L. acknowledges the financial support from the National Natural Science Foundation of China (22373033) and the Wallonie-Bruxelles International (WBI) Excellence scholarship. O.V.P. acknowledges the financial support from the U.S. National Science Foundation (CHE-2154367). The work in Mons was funded by the Belgian National Fund for Scientific Research (FRS-FNRS) within the Consortium des Équipements de Calcul Intensif (CÉCI) under Grant 2.5020.11 and by the Walloon Region (ZENOBE Tier-1 supercomputer) under Grant 1117545. David Beljonne is the FNRS research director. C.Q. is an FNRS research associate. S.G is an FNRS Chargé de recherche.

■ REFERENCES

(1) Sangwan, V. K.; Hersam, M. C. Electronic Transport in Two-Dimensional Materials. *Annu. Rev. Phys. Chem.* **2018**, *69* (1), 299−325.

(2) Brian, D.; Sun, X. Linear-Response and Nonlinear-Response Formulations of the Instantaneous Marcus Theory for Non-equilibrium Photoinduced Charge Transfer. *J. Chem. Theory Comput.* **2021**, *17* (4), 2065−2079.

(3) Jiang, Y.; Geng, H.; Li, W.; Shuai, Z. Understanding Carrier Transport in Organic Semiconductors: Computation of Charge Mobility Considering Quantum Nuclear Tunneling and Delocalization Effects. *J. Chem. Theory Comput.* **2019**, *15* (3), 1477−1491.

(4) Li, X.; Hoffman, J. M.; Kanatzidis, M. G. The 2D Halide Perovskite Rulebook: How the Spacer Influences Everything from the Structure to Optoelectronic Device Efficiency. *Chem. Rev.* **2021**, *121* (4), 2230−2291.

(5) Xie, A.; Maddalena, F.; Witkowski, M. E.; Makowski, M.; Mahler, B.; Drozdowski, W.; Springham, S. V.; Coquet, P.; Dujardin, C.; Birowosuto, M. D.; Dang, C. Library of Two-Dimensional Hybrid Lead Halide Perovskite Scintillator Crystals. *Chem. Mater.* **2020**, *32* (19), 8530−8539.

(6) Sun, C.; Jiang, Y.; Cui, M.; Qiao, L.; Wei, J.; Huang, Y.; Zhang, L.; He, T.; Li, S.; Hsu, H.-Y.; Qin, C.; Long, R.; Yuan, M. High-Performance Large-Area Quasi-2D Perovskite Light-Emitting Diodes. *Nat. Commun.* **2021**, *12* (1), 2207.

(7) Tsai, H.; Nie, W.; Blancon, J.-C.; Stoumpos, C. C.; Soe, C. M. M.; Yoo, J.; Crochet, J.; Tretiak, S.; Even, J.; Sadhanala, A.; Azzellino, G.; Brenes, R.; Ajayan, P. M.; Bulović, V.; Stranks, S. D.; Friend, R. H.; Kanatzidis, M. G.; Mohite, A. D. Stable Light-Emitting Diodes Using Phase-Pure Ruddlesden-Popper Layered Perovskites. *Adv. Mater.* **2018**, *30* (6), 1704217.

(8) Blancon, J.-C.; Even, J.; Stoumpos, C. C.; Kanatzidis, M. G.; Mohite, A. D. Semiconductor Physics of Organic-Inorganic 2D Halide Perovskites. *Nat. Nanotechnol.* **2020**, *15* (12), 969−985.

(9) Li, W.; Sidhik, S.; Traore, B.; Asadpour, R.; Hou, J.; Zhang, H.; Fehr, A.; Essman, J.; Wang, Y.; Hoffman, J. M.; Spanopoulos, I.; Crochet, J. J.; Tsai, E.; Strzalka, J.; Katan, C.; Alam, M. A.; Kanatzidis, M. G.; Even, J.; Blancon, J.-C.; Mohite, A. D. Light-Activated Interlayer Contraction in Two-Dimensional Perovskites for High-Efficiency Solar Cells. *Nat. Nanotechnol.* **2022**, *17* (1), 45−52.

(10) Jiang, Q.; Tong, J.; Xian, Y.; Kerner, R. A.; Dunfield, S. P.; Xiao, C.; Scheidt, R. A.; Kuciauskas, D.; Wang, X.; Hautzinger, M. P.; Tirawat, R.; Beard, M. C.; Fenning, D. P.; Berry, J. J.; Larson, B. W.; Yan, Y.; Zhu, K. Surface Reaction for Efficient and Stable Inverted Perovskite Solar Cells. *Nature* **2022**, *611* (7935), 278−283.

(11) Chattopadhyay, S.; Kokenyesi, R. S.; Hong, M. J.; Watts, C. L.; Labram, J. G. Resolving In-Plane and out-of-Plane Mobility Using

Time Resolved Microwave Conductivity. *J. Mater. Chem. C* **2020**, *8* (31), 10761−10766.
(12) Chao, L.; Niu, T.; Xia, Y.; Ran, X.; Chen, Y.; Huang, W. Efficient and Stable Low-Dimensional Ruddlesden-Popper Perovskite Solar Cells Enabled by Reducing Tunnel Barrier. *J. Phys. Chem. Lett.* **2019**, *10* (6), 1173−1179.
(13) Chen, Y.; Sun, Y.; Peng, J.; Zhang, W.; Su, X.; Zheng, K.; Pullerits, T.; Liang, Z. Tailoring Organic Cation of 2D Air-Stable Organometal Halide Perovskites for Highly Efficient Planar Solar Cells. *Adv. Energy Mater.* **2017**, *7* (18), 1700162.
(14) Tsai, H.; Nie, W.; Blancon, J.-C.; Stoumpos, C. C.; Asadpour, R.; Harutyunyan, B.; Neukirch, A. J.; Verduzco, R.; Crochet, J. J.; Tretiak, S.; Pedesseau, L.; Even, J.; Alam, M. A.; Gupta, G.; Lou, J.; Ajayan, P. M.; Bedzyk, M. J.; Kanatzidis, M. G.; Mohite, A. D. High-Efficiency Two-Dimensional Ruddlesden-Popper Perovskite Solar Cells. *Nature* **2016**, *536* (7616), 312−316.
(15) Lin, Y.; Fang, Y.; Zhao, J.; Shao, Y.; Stuard, S. J.; Nahid, M. M.; Ade, H.; Wang, Q.; Shield, J. E.; Zhou, N.; Moran, A. M.; Huang, J. Unveiling the Operation Mechanism of Layered Perovskite Solar Cells. *Nat. Commun.* **2019**, *10* (1), 1008.
(16) Yu, Z.-G. Omnidirectional Exciton Diffusion in Quasi-2D Hybrid Organic-Inorganic Perovskites. *J. Chem. Phys.* **2022**, *156* (12), 124706.
(17) Katan, C.; Mercier, N.; Even, J. Quantum and Dielectric Confinement Effects in Lower-Dimensional Hybrid Perovskite Semiconductors. *Chem. Rev.* **2019**, *119* (5), 3140−3192.
(18) Passarelli, J. V.; Fairfield, D. J.; Sather, N. A.; Hendricks, M. P.; Sai, H.; Stern, C. L.; Stupp, S. I. Enhanced Out-of-Plane Conductivity and Photovoltaic Performance in n = 1 Layered Perovskites through Organic Cation Design. *J. Am. Chem. Soc.* **2018**, *140* (23), 7313−7323.
(19) Li, X.; Ke, W.; Traoré, B.; Guo, P.; Hadar, I.; Kepenekian, M.; Even, J.; Katan, C.; Stoumpos, C. C.; Schaller, R. D.; Kanatzidis, M. G. Two-Dimensional Dion-Jacobson Hybrid Lead Iodide Perovskites with Aromatic Diammonium Cations. *J. Am. Chem. Soc.* **2019**, *141* (32), 12880−12890.
(20) Gao, Y.; Shi, E.; Deng, S.; Shiring, S. B.; Snaider, J. M.; Liang, C.; Yuan, B.; Song, R.; Janke, S. M.; Liebman-Peláez, A.; Yoo, P.; Zeller, M.; Boudouris, B. W.; Liao, P.; Zhu, C.; Blum, V.; Yu, Y.; Savoie, B. M.; Huang, L.; Dou, L. Molecular Engineering of Organic-Inorganic Hybrid Perovskites Quantum Wells. *Nat. Chem.* **2019**, *11* (12), 1151−1157.
(21) Traore, B.; Pedesseau, L.; Assam, L.; Che, X.; Blancon, J.-C.; Tsai, H.; Nie, W.; Stoumpos, C. C.; Kanatzidis, M. G.; Tretiak, S.; Mohite, A. D.; Even, J.; Kepenekian, M.; Katan, C. Composite Nature of Layered Hybrid Perovskites: Assessment on Quantum and Dielectric Confinements and Band Alignment. *ACS Nano* **2018**, *12* (4), 3321−3332.
(22) Gan, L.; Li, J.; Fang, Z.; He, H.; Ye, Z. Effects of Organic Cation Length on Exciton Recombination in Two-Dimensional Layered Lead Iodide Hybrid Perovskite Crystals. *J. Phys. Chem. Lett.* **2017**, *8* (20), 5177−5183.
(23) Kamminga, M. E.; Fang, H.-H.; Filip, M. R.; Giustino, F.; Baas, J.; Blake, G. R.; Loi, M. A.; Palstra, T. T. M. Confinement Effects in Low-Dimensional Lead Iodide Perovskite Hybrids. *Chem. Mater.* **2016**, *28* (13), 4554−4562.
(24) Li, F.; Xie, Y.; Hu, Y.; Long, M.; Zhang, Y.; Xu, J.; Qin, M.; Lu, X.; Liu, M. Effects of Alkyl Chain Length on Crystal Growth and Oxidation Process of Two-Dimensional Tin Halide Perovskites. *ACS Energy Lett.* **2020**, *5* (5), 1422−1429.
(25) Yu, M.; Yi, C.; Wang, N.; Zhang, L.; Zou, R.; Tong, Y.; Chen, H.; Cao, Y.; He, Y.; Wang, Y.; Xu, M.; Liu, Y.; Jin, Y.; Huang, W.; Wang, J. Control of Barrier Width in Perovskite Multiple Quantum Wells for High Performance Green Light-Emitting Diodes. *Adv. Opt. Mater.* **2019**, *7* (3), 1801575.
(26) Zheng, K.; Chen, Y.; Sun, Y.; Chen, J.; Chábera, P.; Schaller, R.; Al-Marri, M. J.; Canton, S. E.; Liang, Z.; Pullerits, T. Inter-Phase Charge and Energy Transfer in Ruddlesden-Popper 2D Perovskites: Critical Role of the Spacing Cations. *J. Mater. Chem. A* **2018**, *6* (15), 6244−6250.
(27) Liu, J.; Leng, J.; Wu, K.; Zhang, J.; Jin, S. Observation of Internal Photoinduced Electron and Hole Separation in Hybrid Two-Dimentional Perovskite Films. *J. Am. Chem. Soc.* **2017**, *139* (4), 1432−1435.
(28) Yuan, M.; Quan, L. N.; Comin, R.; Walters, G.; Sabatini, R.; Voznyy, O.; Hoogland, S.; Zhao, Y.; Beauregard, E. M.; Kanjanaboos, P.; Lu, Z.; Kim, D. H.; Sargent, E. H. Perovskite Energy Funnels for Efficient Light-Emitting Diodes. *Nat. Nanotechnol.* **2016**, *11* (10), 872−877.
(29) Zhang, F.; Kim, D. H.; Lu, H.; Park, J.-S.; Larson, B. W.; Hu, J.; Gao, L.; Xiao, C.; Reid, O. G.; Chen, X.; Zhao, Q.; Ndione, P. F.; Berry, J. J.; You, W.; Walsh, A.; Beard, M. C.; Zhu, K. Enhanced Charge Transport in 2D Perovskites via Fluorination of Organic Cation. *J. Am. Chem. Soc.* **2019**, *141* (14), 5972−5979.
(30) Xu, Z.; Chen, M.; Liu, S. F. First-Principles Study of Enhanced Out-of-Plane Transport Properties and Stability in Dion-Jacobson Two-Dimensional Perovskite Semiconductors for High-Performance Solar Cell Applications. *J. Phys. Chem. Lett.* **2019**, *10* (13), 3670−3675.
(31) Fang, Z.; Hou, X.; Zheng, Y.; Yang, Z.; Chou, K.-C.; Shao, G.; Shang, M.; Yang, W.; Wu, T. First-Principles Optimization of Out-of-Plane Charge Transport in Dion-Jacobson CsPbI3 Perovskites with π-Conjugated Aromatic Spacers. *Adv. Funct. Mater.* **2021**, *31* (28), 2102330.
(32) Mosconi, E.; Alothman, A. A.; Long, R.; Kaiser, W.; De Angelis, F. Intermolecular Interactions of A-Site Cations Modulate Stability of 2D Metal Halide Perovskites. *ACS Energy Lett.* **2023**, *8*, 748−752.
(33) Quarti, C.; Marchal, N.; Beljonne, D. Tuning the Optoelectronic Properties of Two-Dimensional Hybrid Perovskite Semiconductors with Alkyl Chain Spacers. *J. Phys. Chem. Lett.* **2018**, *9* (12), 3416−3424.
(34) Marchal, N.; Mosconi, E.; García-Espejo, G.; Almutairi, T. M.; Quarti, C.; Beljonne, D.; De Angelis, F. Cation Engineering for Resonant Energy Level Alignment in Two-Dimensional Lead Halide Perovskites. *J. Phys. Chem. Lett.* **2021**, *12*, 2528−2535.
(35) Jahanbakhshi, F.; Mladenović, M.; Dankl, M.; Boziki, A.; Ahlawat, P.; Rothlisberger, U. Organic Spacers in 2D Perovskites: General Trends and Structure-Property Relationships from Computational Studies. *Helv. Chim. Acta* **2021**, *104* (4), No. e2000232.
(36) Quan, J.; Yu, S.; Xing, B.; He, X.; Zhang, L. Two-Dimensional Ruddlesden-Popper Halide Perovskite Solar Absorbers with Short-Chain Interlayer Spacers. *Phys. Rev. Mater.* **2022**, *6* (6), 065405.
(37) Proppe, A. H.; Elkins, M. H.; Voznyy, O.; Pensack, R. D.; Zapata, F.; Besteiro, L. V.; Quan, L. N.; Quintero-Bermudez, R.; Todorovic, P.; Kelley, S. O.; Govorov, A. O.; Gray, S. K.; Infante, I.; Sargent, E. H.; Scholes, G. D. Spectrally Resolved Ultrafast Exciton Transfer in Mixed Perovskite Quantum Wells. *J. Phys. Chem. Lett.* **2019**, *10* (3), 419−426.
(38) Oberhofer, H.; Reuter, K.; Blumberger, J. Charge Transport in Molecular Materials: An Assessment of Computational Methods. *Chem. Rev.* **2017**, *117* (15), 10319−10357.
(39) Futera, Z.; Blumberger, J. Electronic Couplings for Charge Transfer across Molecule/Metal and Molecule/Semiconductor Interfaces: Performance of the Projector Operator-Based Diabatization Approach. *J. Phys. Chem. C* **2017**, *121* (36), 19677−19689.
(40) Kondov, I.; Čížek, M.; Benesch, C.; Wang, H.; Thoss, M. Quantum Dynamics of Photoinduced Electron-Transfer Reactions in Dye-Semiconductor Systems: First-Principles Description and Application to Coumarin 343-TiO2. *J. Phys. Chem. C* **2007**, *111* (32), 11970−11981.
(41) Ozaki, T. Variationally Optimized Atomic Orbitals for Large-Scale Electronic Structures. *Phys. Rev. B* **2003**, *67* (15), 155108.
(42) Ozaki, T.; Kino, H. Numerical Atomic Basis Orbitals from H to Kr. *Phys. Rev. B* **2004**, *69* (19), 195113.
(43) Billing, D. G.; Lemmerer, A. Synthesis, Characterization and Phase Transitions of the Inorganic-Organic Layered Perovskite-Type

https://doi.org/10.1021/acs.jctc.3c00904
J. Chem. Theory Comput. 2023, 19, 9403−9415

Hybrids [(CnH2n+1NH3)2PbI4] (n = 12, 14, 16 and 18). *New J. Chem.* **2008**, *32* (10), 1736−1746.
(44) Billing, D. G.; Lemmerer, A. Synthesis, Characterization and Phase Transitions in the Inorganic-Organic Layered Perovskite-Type Hybrids [(CnH2n + 1NH3)2PbI4], n = 4, 5 and 6. *Acta Crystallogr. Sect. B* **2007**, *63* (5), 735−747.
(45) Lemmerer, A.; Billing, D. G. Synthesis, Characterization and Phase Transitions of the Inorganic-Organic Layered Perovskite-Type Hybrids [(CnH2n+1NH3)2PbI4], n = 7, 8, 9 and 10. *Dalton Trans.* **2012**, *41* (4), 1146−1157.
(46) Lambert, C.; Nöll, G.; Schelter, J. Bridge-Mediated Hopping or Superexchange Electron-Transfer Processes in Bis(Triarylamine) Systems. *Nat. Mater.* **2002**, *1* (1), 69−73.
(47) Marcus, R. A. On the Theory of Chemiluminescent Electron-Transfer Reactions. *J. Chem. Phys.* **1965**, *43* (8), 2654−2657.
(48) Coropceanu, V.; Cornil, J.; da Silva Filho, D. A.; Olivier, Y.; Silbey, R.; Brédas, J.-L. Charge Transport in Organic Semiconductors. *Chem. Rev.* **2007**, *107* (4), 926−952.
(49) Blumberger, J. Recent Advances in the Theory and Molecular Simulation of Biological Electron Transfer Reactions. *Chem. Rev.* **2015**, *115* (20), 11191−11238.
(50) Neukirch, A. J.; Abate, I. I.; Zhou, L.; Nie, W.; Tsai, H.; Pedesseau, L.; Even, J.; Crochet, J. J.; Mohite, A. D.; Katan, C.; Tretiak, S. Geometry Distortion and Small Polaron Binding Energy Changes with Ionic Substitution in Halide Perovskites. *J. Phys. Chem. Lett.* **2018**, *9* (24), 7130−7136.
(51) Neukirch, A. J.; Nie, W.; Blancon, J.-C.; Appavoo, K.; Tsai, H.; Sfeir, M. Y.; Katan, C.; Pedesseau, L.; Even, J.; Crochet, J. J.; Gupta, G.; Mohite, A. D.; Tretiak, S. Polaron Stabilization by Cooperative Lattice Distortion and Cation Rotations in Hybrid Perovskite Materials. *Nano Lett.* **2016**, *16* (6), 3809−3816.
(52) Blumberger, J.; Lamoureux, G. Reorganization Free Energies and Quantum Corrections for a Model Electron Self-Exchange Reaction: Comparison of Polarizable and Non-Polarizable Solvent Models. *Mol. Phys.* **2008**, *106* (12−13), 1597−1611.
(53) Yangui, A.; Sy, M.; Li, L.; Abid, Y.; Naumov, P.; Boukheddaden, K. Rapid and Robust Spatiotemporal Dynamics of the First-Order Phase Transition in Crystals of the Organic-Inorganic Perovskite (C12H25NH3)2PbI4. *Sci. Rep.* **2015**, *5* (1), 16634.
(54) Ghosh, D.; Acharya, D.; Pedesseau, L.; Katan, C.; Even, J.; Tretiak, S.; Neukirch, A. J. Charge Carrier Dynamics in Two-Dimensional Hybrid Perovskites: Dion-Jacobson vs. Ruddlesden-Popper Phases. *J. Mater. Chem. A* **2020**, *8*, 22009−22022.
(55) Zhang, Z.; Fang, W.-H.; Tokina, M. V.; Long, R.; Prezhdo, O. V. Rapid Decoherence Suppresses Charge Recombination in Multi-Layer 2D Halide Perovskites: Time-Domain Ab Initio Analysis. *Nano Lett.* **2018**, *18* (4), 2459−2466.
(56) Kresse, G.; Hafner, J. *Ab Initio* Molecular Dynamics for Liquid Metals. *Phys. Rev. B* **1993**, *47* (1), 558−561.
(57) Grimme, S. Semiempirical GGA-Type Density Functional Constructed with a Long-Range Dispersion Correction. *J. Comput. Chem.* **2006**, *27* (15), 1787−1799.
(58) Perdew, J. P.; Burke, K.; Ernzerhof, M. Generalized Gradient Approximation Made Simple. *Phys. Rev. Lett.* **1996**, *77* (18), 3865−3868.
(59) Li, W.; Zhou, L.; Prezhdo, O. V.; Akimov, A. V. Spin-Orbit Interactions Greatly Accelerate Nonradiative Dynamics in Lead Halide Perovskites. *ACS Energy Lett.* **2018**, *3* (9), 2159−2166.
(60) Smith, B.; Shakiba, M.; Akimov, A. V. Nonadiabatic Dynamics in Si and CdSe Nanoclusters: Many-Body vs Single-Particle Treatment of Excited States. *J. Chem. Theory Comput.* **2021**, *17* (2), 678−693.
(61) Shakiba, M.; Stippell, E.; Li, W.; Akimov, A. V. Nonadiabatic Molecular Dynamics with Extended Density Functional Tight-Binding: Application to Nanocrystals and Periodic Solids. *J. Chem. Theory Comput.* **2022**, *18* (9), 5157−5180.
(62) Ishihara, T.; Takahashi, J.; Goto, T. Optical Properties Due to Electronic Transitions in Two-Dimensional Semiconductors (CnH2n+1NH3)2PbI4. *Phys. Rev. B Condens. Matter* **1990**, *42* (17), 11099−11107.
(63) Pedesseau, L.; Sapori, D.; Traore, B.; Robles, R.; Fang, H.-H.; Loi, M. A.; Tsai, H.; Nie, W.; Blancon, J.-C.; Neukirch, A.; Tretiak, S.; Mohite, A. D.; Katan, C.; Even, J.; Kepenekian, M. Advances and Promises of Layered Halide Hybrid Perovskite Semiconductors. *ACS Nano* **2016**, *10* (11), 9776−9786.
(64) Yang, L.; Chen, Y.; Wang, X.; Deng, J.; Wang, W.; Ding, X.; Yang, W.; Yao, J. First-Principles Study on the Stability and Electronic Properties of Dion-Jacobson Halide A′(MA)N-1BnX3n+1 Perovskites. *J. Phys. Chem. C* **2021**, *125*, 24096.
(65) Quarti, C.; Katan, C.; Even, J. Physical Properties of Bulk, Defective, 2D and 0D Metal Halide Perovskite Semiconductors from a Symmetry Perspective. *J. Phys. Mater.* **2020**, *3* (4), 042001.
(66) Moral, R. F.; Germino, J. C.; Bonato, L. G.; Almeida, D. B.; Therézio, E. M.; Atvars, T. D. Z.; Stranks, S. D.; Nome, R. A.; Nogueira, A. F. Influence of the Vibrational Modes from the Organic Moieties in 2D Lead Halides on Excitonic Recombination and Phase Transition. *Adv. Opt. Mater.* **2020**, *8* (24), 2001431.
(67) Lavan, S. N.; Sanni, A. M.; Rury, A. S.; Liu, Z.-F. Characterization of the Ammonium Bending Vibrations in Two-Dimensional Hybrid Lead-Halide Perovskites from Raman Spectroscopy and First-Principles Calculations. *J. Phys. Chem. C* **2021**, *125* (1), 223−236.
(68) Thouin, F.; Valverde-Chávez, D. A.; Quarti, C.; Cortecchia, D.; Bargigia, I.; Beljonne, D.; Petrozza, A.; Silva, C.; Srimath Kandada, A. R. Phonon Coherences Reveal the Polaronic Character of Excitons in Two-Dimensional Lead Halide Perovskites. *Nat. Mater.* **2019**, *18* (4), 349−356.
(69) Menahem, M.; Dai, Z.; Aharon, S.; Sharma, R.; Asher, M.; Diskin-Posner, Y.; Korobko, R.; Rappe, A. M.; Yaffe, O. Strongly Anharmonic Octahedral Tilting in Two-Dimensional Hybrid Halide Perovskites. *ACS Nano* **2021**, *15* (6), 10153−10162.
(70) Dhanabalan, B.; Leng, Y.-C.; Biffi, G.; Lin, M.-L.; Tan, P.-H.; Infante, I.; Manna, L.; Arciniegas, M. P.; Krahne, R. Directional Anisotropy of the Vibrational Modes in 2D-Layered Perovskites. *ACS Nano* **2020**, *14* (4), 4689−4697.
(71) Dahod, N. S.; France-Lanord, A.; Paritmongkol, W.; Grossman, J. C.; Tisdale, W. A. Low-Frequency Raman Spectrum of 2D Layered Perovskites: Local Atomistic Motion or Superlattice Modes? *J. Chem. Phys.* **2020**, *153* (4), 044710.
(72) Chen, Y.-F.; Mahata, A.; Lubio, A. D.; Cinquino, M.; Coriolano, A.; Skokan, L.; Jeong, Y.-G.; Razzari, L.; De Marco, L.; Ruediger, A.; De Angelis, F.; Colella, S.; Orgiu, E. Phonon Analysis of 2D Organic-Halide Perovskites in the Low- and Mid-IR Region. *Adv. Opt. Mater.* **2022**, *10* (16), 2100439.
(73) Lekina, Y.; Dintakurti, S. S. H.; Febriansyah, B.; Bradley, D.; Yan, J.; Shi, X.; England, J.; White, T.; Hanna, J. V.; Shen, Z. X. The Effect of Organic Cation Dynamics on the Optical Properties in (PEA)2(MA)[Pb2I7] Perovskite Dimorphs. *J. Mater. Chem. C* **2021**, *9* (47), 17050−17060.
(74) Sanni, A. M.; Lavan, S. N.; Rury, A. S. Anharmonic Molecular Vibrational Probes of Dynamical Organic-Inorganic Interactions in Two-Dimensional Hybrid Lead Iodide Perovskites. *J. Phys. Chem. C* **2020**, *124* (25), 13942−13955.
(75) Giannini, S.; Carof, A.; Ellis, M.; Yang, H.; Ziogos, O. G.; Ghosh, S.; Blumberger, J. Quantum Localization and Delocalization of Charge Carriers in Organic Semiconducting Crystals. *Nat. Commun.* **2019**, *10*, No. 3843, DOI: 10.1038/s41467-019-11775-9.
(76) Frohna, K.; Deshpande, T.; Harter, J.; Peng, W.; Barker, B. A.; Neaton, J. B.; Louie, S. G.; Bakr, O. M.; Hsieh, D.; Bernardi, M. Inversion Symmetry and Bulk Rashba Effect in Methylammonium Lead Iodide Perovskite Single Crystals. *Nat. Commun.* **2018**, *9* (1), 1829.
(77) Jana, M. K.; Song, R.; Xie, Y.; Zhao, R.; Sercel, P. C.; Blum, V.; Mitzi, D. B. Structural Descriptor for Enhanced Spin-Splitting in 2D Hybrid Perovskites. *Nat. Commun.* **2021**, *12* (1), 4982.

(78) Boström, H. L. B.; Senn, M. S.; Goodwin, A. L. Recipes for Improper Ferroelectricity in Molecular Perovskites. *Nat. Commun.* **2018**, *9* (1), 2380.
(79) Berlin, Y. A.; Burin, A. L.; Ratner, M. A. Charge Hopping in DNA. *J. Am. Chem. Soc.* **2001**, *123* (2), 260−268.
(80) Beljonne, D.; Pourtois, G.; Ratner, M. A.; Brédas, J. L. Pathways for Photoinduced Charge Separation in DNA Hairpins. *J. Am. Chem. Soc.* **2003**, *125* (47), 14510−14517.
(81) Tsuji, Y.; Movassagh, R.; Datta, S.; Hoffmann, R. Exponential Attenuation of Through-Bond Transmission in a Polyene: Theory and Potential Realizations. *ACS Nano* **2015**, *9* (11), 11109−11120.
(82) Bixon, M.; Jortner, J. Electron Transfer—from Isolated Molecules to Biomolecules. In *Advances in Chemical Physics*; Prigogine, I., Rice, S. A., Eds.; John Wiley & Sons, Hoboken, New Jersey, U.S., 2007; p 35−202. DOI: 10.1002/9780470141656.ch3.
(83) Giannini, S.; Blumberger, J. Charge Transport in Organic Semiconductors: The Perspective from Nonadiabatic Molecular Dynamics. *Acc. Chem. Res.* **2022**, *55* (6), 819−830.
(84) Prodhan, S.; Giannini, S.; Wang, L.; Beljonne, D. Long-Range Interactions Boost Singlet Exciton Diffusion in Nanofibers of π-Extended Polymer Chains. *J. Phys. Chem. Lett.* **2021**, *12* (34), 8188−8193.
(85) Wang, Y.; Pedesseau, L.; Katan, C.; Even, J.; Prezhdo, O. V.; Tretiak, S.; Ghosh, D.; Neukirch, A. J. Nonadiabatic Molecular Dynamics Analysis of Hybrid Dion-Jacobson 2D Leads Iodide Perovskites. *Appl. Phys. Lett.* **2021**, *119* (20), 201102.
(86) Giannini, S.; Carof, A.; Blumberger, J. Crossover from Hopping to Band-Like Charge Transport in an Organic Semiconductor Model: Atomistic Nonadiabatic Molecular Dynamics Simulation. *J. Phys. Chem. Lett.* **2018**, *9* (11), 3116−3123.
(87) Duhm, S.; Xin, Q.; Hosoumi, S.; Fukagawa, H.; Sato, K.; Ueno, N.; Kera, S. Charge Reorganization Energy and Small Polaron Binding Energy of Rubrene Thin Films by Ultraviolet Photoelectron Spectroscopy. *Adv. Mater.* **2012**, *24* (7), 901−905.
(88) Gruhn, N. E.; da Silva Filho, D. A.; Bill, T. G.; Malagoli, M.; Coropceanu, V.; Kahn, A.; Brédas, J.-L. The Vibrational Reorganization Energy in Pentacene: Molecular Influences on Charge Transport. *J. Am. Chem. Soc.* **2002**, *124* (27), 7918−7919.
(89) Neukirch, A. J.; Nie, W.; Blancon, J.-C.; Appavoo, K.; Tsai, H.; Sfeir, M. Y.; Katan, C.; Pedesseau, L.; Even, J.; Crochet, J. J.; Gupta, G.; Mohite, A. D.; Tretiak, S. Polaron Stabilization by Cooperative Lattice Distortion and Cation Rotations in Hybrid Perovskite Materials. *Nano Lett.* **2016**, *16* (6), 3809−3816.
(90) Elsner, J.; Giannini, S.; Blumberger, J. Mechanoelectric Response of Single-Crystal Rubrene from Ab Initio Molecular Dynamics. *J. Phys. Chem. Lett.* **2021**, *12* (25), 5857−5863.
(91) Biega, R.-I.; Bokdam, M.; Herrmann, K.; Mohanraj, J.; Skrybeck, D.; Thelakkat, M.; Retsch, M.; Leppert, L. Dynamic Distortions of Quasi-2D Ruddlesden-Popper Perovskites at Elevated Temperatures: Influence on Thermal and Electronic Properties. *J. Phys. Chem. C* **2023**, *127*, 9183−9195.
(92) Zhang, Z.; Fang, W.-H.; Long, R.; Prezhdo, O. V. Exciton Dissociation and Suppressed Charge Recombination at 2D Perovskite Edges: Key Roles of Unsaturated Halide Bonds and Thermal Disorder. *J. Am. Chem. Soc.* **2019**, *141* (39), 15557−15566.
(93) Stafström, S. Electron Localization and the Transition from Adiabatic to Nonadiabatic Charge Transport in Organic Conductors. *Chem. Soc. Rev.* **2010**, *39* (7), 2484−2499.
(94) Troisi, A. Charge Transport in High Mobility Molecular Semiconductors: Classical Models and New Theories. *Chem. Soc. Rev.* **2011**, *40* (5), 2347−2358.
(95) Troisi, A. The Speed Limit for Sequential Charge Hopping in Molecular Materials. *Org. Electron.* **2011**, *12* (12), 1988−1991.
(96) Li, C.; Yang, J.; Su, F.; Tan, J.; Luo, Y.; Ye, S. Conformational Disorder of Organic Cations Tunes the Charge Carrier Mobility in Two-Dimensional Organic-Inorganic Perovskites. *Nat. Commun.* **2020**, *11* (1), 5481.
(97) Wang, L.; Prezhdo, O. V.; Beljonne, D. Mixed Quantum-Classical Dynamics for Charge Transport in Organics. *Phys. Chem. Chem. Phys.* **2015**, *17* (19), 12395−12406.
(98) Mayers, M. Z.; Tan, L. Z.; Egger, D. A.; Rappe, A. M.; Reichman, D. R. How Lattice and Charge Fluctuations Control Carrier Dynamics in Halide Perovskites. *Nano Lett.* **2018**, *18*, 8041.
(99) Milot, R. L.; Eperon, G. E.; Snaith, H. J.; Johnston, M. B.; Herz, L. M. Temperature-Dependent Charge-Carrier Dynamics in CH3NH3PbI3 Perovskite Thin Films. *Adv. Funct. Mater.* **2015**, *25* (39), 6218−6227.
(100) Gélvez-Rueda, M. C.; Hutter, E. M.; Cao, D. H.; Renaud, N.; Stoumpos, C. C.; Hupp, J. T.; Savenije, T. J.; Kanatzidis, M. G.; Grozema, F. C. Interconversion between Free Charges and Bound Excitons in 2D Hybrid Lead Halide Perovskites. *J. Phys. Chem. C* **2017**, *121* (47), 26566−26574.
(101) Seitz, M.; Magdaleno, A. J.; Alcázar-Cano, N.; Meléndez, M.; Lubbers, T. J.; Walraven, S. W.; Pakdel, S.; Prada, E.; Delgado-Buscalioni, R.; Prins, F. Exciton Diffusion in Two-Dimensional Metal-Halide Perovskites. *Nat. Commun.* **2020**, *11* (1), 2035.
(102) Nazarenko, O.; Kotyrba, M. R.; Wörle, M.; Cuervo-Reyes, E.; Yakunin, S.; Kovalenko, M. V. Luminescent and Photoconductive Layered Lead Halide Perovskite Compounds Comprising Mixtures of Cesium and Guanidinium Cations. *Inorg. Chem.* **2017**, *56* (19), 11552−11564.
(103) Sourisseau, S.; Louvain, N.; Bi, W.; Mercier, N.; Rondeau, D.; Boucher, F.; Buzaré, J.-Y.; Legein, C. Reduced Band Gap Hybrid Perovskites Resulting from Combined Hydrogen and Halogen Bonding at the Organic-Inorganic Interface. *Chem. Mater.* **2007**, *19* (3), 600−607.
(104) Sidhik, S.; Wang, Y.; De Siena, M.; Asadpour, R.; Torma, A. J.; Terlier, T.; Ho, K.; Li, W.; Puthirath, A. B.; Shuai, X.; Agrawal, A.; Traore, B.; Jones, M.; Giridharagopal, R.; Ajayan, P. M.; Strzalka, J.; Ginger, D. S.; Katan, C.; Alam, M. A.; Even, J.; Kanatzidis, M. G.; Mohite, A. D. Deterministic Fabrication of 3D/2D Perovskite Bilayer Stacks for Durable and Efficient Solar Cells. *Science* **2022**, *377* (6613), 1425−1430.
(105) Blancon, J.-C.; Stier, A. V.; Tsai, H.; Nie, W.; Stoumpos, C. C.; Traoré, B.; Pedesseau, L.; Kepenekian, M.; Katsutani, F.; Noe, G. T.; Kono, J.; Tretiak, S.; Crooker, S. A.; Katan, C.; Kanatzidis, M. G.; Crochet, J. J.; Even, J.; Mohite, A. D. Scaling Law for Excitons in 2D Perovskite Quantum Wells. *Nat. Commun.* **2018**, *9* (1), 2254.

NOTE ADDED AFTER ASAP PUBLICATION

This paper was published ASAP on December 4, 2023, with an error in equation 12. The corrected version was reposted on December 5, 2023.

https://doi.org/10.1021/acs.jctc.3c00904
J. Chem. Theory Comput. 2023, 19, 9403−9415